ELSEVIER

Journal of Alloys and Compounds 262–263 (1997) 1–9

Journal of ALLOYS AND COMPOUNDS

# Localized-itinerant electronic transitions in oxides and sulfides

J.B. Goodenough*

*Center for Materials Science and Engineering, ETC 9.102, University of Texas at Austin, Austin, TX 78712-1063, USA*

**Abstract**

Comparison of the transition-metal oxides and sulfides highlights as a common feature the possibility of finding a displacive crystallographic transition at a cross-over from localized to itinerant electronic behavior. In metastable NiS with the $B8_1$ structure, for example, this cross-over manifests itself as a first-order expansion of the $c$-axis on cooling from a Pauli-paramagnetic metallic phase to an antiferromagnetic phase at a Néel temperature $T_N = 264$ K. A first-order lattice expansion also occurs in the perovskite $NdNiO_3$ on cooling from a metallic to an insulating phase, but in this case the magnetic order below $T_N$ indicates a segregation into ferromagnetic Ni–O–Ni (111) sheets containing itinerant electrons that are coupled by ionic bonding across an oxide-ion (111) plane to give a charge-density wave (CDW) with a propagation vector $\mathbf{q}_{CDW}$ [111] and a spin-density wave (SDW) with $\mathbf{q}_{SDW} \approx 2\mathbf{q}_{CDW}$. In rhombohedral FeS, itinerant minority-spin electrons co-exist with localized majority-spin electrons into molecular orbitals. A low-spin to intermediate-spin transition in $LaCoO_3$ occurs via short-range ordering of low-spin and high-spin to intermediate-spin trivalent cobalt, localized e electrons at the high-spin cobalt transforming to itinerant $\sigma^*$ electrons in the intermediate spin state. As a final example, mixed-valent manganese oxides with perovskite structure are chosen to illustrate strong electron coupling to local Jahn–Teller deformations at a cross-over from localized to itinerant electronic behavior of $\sigma$-bonding electrons in the presence of $\pi$-bonding electron configurations with localized spins $S = 3/2$. 

*Keywords:* Phase transitions; Electron transitions; Localized to itinerant; Perovskites; Sulfides

## 1. Oxides versus sulfides

The departure this year from the traditional exclusion from the program of transition-metal oxides makes it appropriate to open this conference with a brief review of the principal features that distinguish the oxides from the chalcogenide closest to an oxide ion; comparison is restricted to oxides and sulfides.

Fig. 1 shows a schematic construction of the electronic energies for MnO starting from an ionic model. The energy $E_I = E_i - E_A$ is the energy required to create isolated $Mn^{2+}$ and $O^{2-}$ ions; $E_i$ is the ionization energy for removal of an electron from a $Mn^+$ ion to vacuum and $E_A < 0$ is the energy to add an electron to an $O^-$ ion. The $O^{2-}$ ion is stabilized by the electrostatic crystalline field generated by assembling the ions into the rock-salt structure. The total electrostatic Madelung energy

$$E_m \sim (z_e)^2/R \tag{1}$$

is partitioned by the conservation of energy so as to the lower $O^{2-}$ ion energy level by $E_m/2$ and raise the $Mn^{2+}$ energy levels by $E_m/2$. In Eq. (1), $R$ is the equilibrium Mn–O bond length and $z = 2$ for a point-charge ionic model. An $E_m - E_I > 0$ results in a crossing of the $Mn^{2+}$ and $O^{2-}$ energies. The covalent introduction of electron transfer from the $O^{2-}$ ions

* Corresponding author.

0925-8388/97/$17.00 
*PII* S0925-8388(97)00321-6

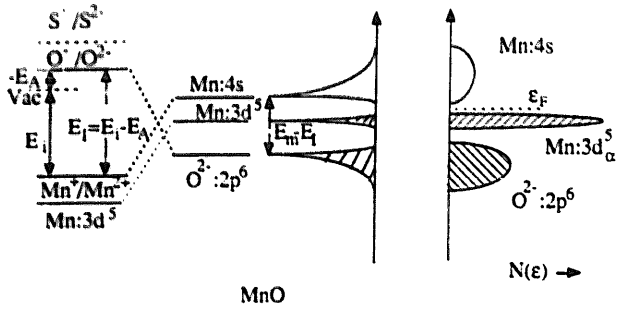


Fig. 1. Schematic construction of electronic energies for MnO starting from an ionic model.

back to the empty states at an $Mn^{2+}$ ion may be treated in second-order perturbation theory so long as the energy $\Delta E$ between these states is sufficiently large. The associated loss in the effective ionic charge $z_e$, which lowers $E_m$, is compensated by the quantum-mechanical admixture of Mn-4s and O-2p states; this state mixing raises the antibonding, primarily $Mn^{2+}$:$4s^0$ level and lowers the bonding, primarily $O^{2-}$:$2p^6$ energy. The interatomic interactions between the neighbors also broaden these energies into a conduction band of primarily $Mn^{2+}$:4s character and a valence band of primarily $O^{2-}$:$2p^6$ character with an energy density $N(\epsilon)$ of one-electron states of energy $\epsilon$.

In MnO, the crystalline field at a cation also raises the energy of the high-spin $Mn^{2+}$:$3d^5_u$ configuration into the energy gap $E_g$ between the bottom of the 4s conduction band and the top of the $2p^6$ valence band. Weak interactions between the Mn atoms leave the $3d^5_u$ electrons localized; their interactions may be described by the superexchange perturbation theory.

Location of the Mn:$3d^5_u$ energy with the gap $E_g$ allows oxidation of the $Mn^{2+}$ ion to $Mn^{3+}$ in an oxide; lowering the Fermi energy $E_F$ through the $Mn^{3+}/Mn^{2+}$ redox couple, i.e. through the $3d^5_u$ level, leaves $\epsilon_F$ still within $E_g$. Moreover, location within $E_g$ of the subsequent $Mn^{4+}/Mn^{3+}$ couple corresponding to $3d^4_u$ allows a further oxidation of the cation to $Mn^{4+}$ in $MnO_2$. In $MnO_2$, a relatively small energy $\Delta E$ between the $O^{2-}$:$2p^6$ and empty $Mn^{4+}$:$3d^4_u$ energies of the point-charge ionic model introduces a stronger covalent mixing of the Mn-3d and O-2p states. Where $\Delta E$ becomes too small, an ionic model with covalent admixture treated in second-order perturbation theory needs to be replaced by an ab initio band model and the 3d electrons may become itinerant.

The electron affinity, $E_A$, of the sulfide ion is even more negative than that of the oxide ion, which increased $E_i$ for MnS. Moreover, the larger size of the $S^{2-}$ ion increases the equilibrium MnS bond length $R$. The resulting decrease in $E_m - E_i$ results in a smaller band gap $E_g$ between the $S^{2-}$:$3p^6$ valence band and the $Mn^{2+}$:4s conduction band in MnS. As a result, the crystalline fields do not raise the Mn:$3d^5_\alpha$ level into the gap $E_g$, so it is not possible to access as $Mn^{3+}$:$3d^4_\alpha$ localized electron neighboring $Mn^{2+}$ ions are weak enough that they may be treated in second-order superexchange theory. MnS is an antiferromagnetic insulator like MnO. On the other hand, oxidation of MnS of $MnS_2$ results in oxidation of the $S^{2-}$ ions to give the disulfide $(S_2)^{2-}$ ions with $Mn^{2+}$; the $Mn^{4+}$ ion is not accessible in a sulfide [1].

From these simple considerations, it follows that the energy gap $E_g$ between a transition-metal 4s conduction band and an $S^2$:$3p^6$ valence band is smaller than that for and $O^2$:$2p^6$ valence band in oxide. A consequence of this reduction in $E_g$ is an inaccessibility in sulfides of the higher valence states found in the oxides and a smaller energy $\Delta E$ to empty states for a given formal valence state of the cation; the result is a stronger covalent mixing in the sulfides, a more common breakdown of the ionic model and a more common formation of disulfide ions than peroxide ions.

In addition, a smaller intraatomic energy separation $\Delta E_a$ of the $3d^0$ from the $3p^6$ energies in a sulfide ion compared to the separation of the $3s^0$ from the $2p^6$ energies of an oxide ion means that the Van der Waals bonding between two sulfide ions is stronger than that between two oxide ions. The virtual charge transfer between two anions that gives rise to this Van der Waals bonding is described by a second-order perturbation theory and hence is inversely proportional $\Delta E_a$. Thus $TiS_2$ forms strongly bonded $TiS_2$ sandwich layers bonded to one another by S–S Van der Waals bonding whereas $TiO_2$ forms a three-dimensional network of strong Ti–O bonds. Moreover, accessibility of the $3d^0$ states at a sulfide ion may stabilize $S^{2-}$ in a trigonal-prismatic coordination of cations whereas sixfold cation coordination at an oxide ion is invariably based on an octahedral configuration. These factors plus the stronger metal-sulfide covalent mixing and the larger size of the sulfide ion result in structures in the sulfides quite different from those found in oxides and classify the sulfides as one of the chalcogenides forming compounds distinguishable from the oxides.

Nevertheless, there is one property that is found in both oxides and sulfides that is at the center of considerable research effort, i.e. the possibility of observing transitions from localized to itinerant 3d-electron behavior occurring at temperatures where only displacive crystallographic transitions are possible. Five examples of such transitions are chosen for illustration.

## 2. Localized-itinerant electron transitions

The Virial Theorem of classical mechanics states that, for central-force fields,

$$2\langle T\rangle + \langle V\rangle = 0 \quad (2)$$

where $\langle T\rangle$ is the mean kinetic energy of a system and $\langle V\rangle$ is its mean potential energy [2]. If the mean kinetic energy of an electronic system varies discontinuously at a transition for localized to itinerant behavior, then the mean potential energy must also change discontinuously. A discontinuous change in the $\langle V\rangle$ of an electronic system requires a discontinuous change in the mean equilibrium metal-anion bond length, which in turn means that the transition must be first-order. For antibonding 3d electrons, a decrease in $\langle V\rangle$ would be reflected in a decrease in the mean metal-anion bond length, $\langle$M–X$\rangle$. Since we may anticipate a discontinuous increase in $\langle T\rangle$ on crossing from localized to itinerant electronic behavior, it follows that

$$\langle \text{M–X}\rangle_{\text{local}} > \langle \text{M–X}\rangle_{\text{itin}} \quad (3)$$

and therefore that a decrease in volume, $\Delta V < 0$, would accompany a transition from localized to itinerant electronic behavior. It also follows from Eq. (3) that hydrostatic pressure $P$ would favor the itinerant-electron phase and that the $\langle$M–X$\rangle_{\text{local}}$ bond length should have an anomalously high compressibility near the transition where the equilibrium bond length experiences a double-well potential.

It should be noted that a first-order localized-itinerant electronic transition does not require a change in lattice symmetry; it may be accommodated by a simple change of volume with no symmetry change. On the other hand, first-order transitions commonly occur via a two-phase regime within a range of the variable (temperature, pressure, composition) over which the transition occurs. If the transition temperature $T_t$ is too low for phase segregation to occur via atomic diffusion, a separation into domains where the electrons occupy localized states and those where they occupy molecular orbitals or itinerant-electron states may nevertheless be stabilized by cooperative atomic displacements. Moreover, the cooperative atomic displacements may be either static or dynamic. Long-range cooperativity generally results in static displacements that change the translational and/or space-group symmetry; long-range, static displacements are readily detected by conventional X-ray or neutron diffraction. More subtle and not generally recognized are examples where the phase segregation is short-range and dynamic. Short-range cooperatively resulting in dynamic phase segregation is more likely to occur in a mixed-valent composition.

## 3. Nickel sulfide

NiS is a metallic compound that transforms on cooling through 650°C from the hexagonal $B8_1$ structure of NiAs to the peculiar Millerite structure. However, the $B8_1$ phase can be retained to low temperatures by quenching to room temperature from above 650°C [3a,3b]. Below room temperature atomic diffusion is suppressed, but a first-order, endothermic $B8_1 = B8_1$ transition occurs at a $T_N = 264$ K, the $c$-axis expanding discontinuously by 0.06 Å on cooling through $T_N$ with only a small change from symmetry $P6_3/mmc$ to $P6_3/mc$ due to a small shift of the cation array relative to the anion array [4]. Above $T_N$, the compound remains metallic and Pauli paramagnetic; below $T_N$ it is a semimetallic antiferromagnet with a nickel atomic moment $\mu_{Ni} \approx 1.6\ \mu_B$. The resistivity increases by a factor of 40 on cooling through $T_N$.

Clearly a transition from strongly to weakly correlated electrons, i.e. from more localized to itinerant electronic behavior, occurs at $T_N$, so we should expect hydrostatic pressure to suppress strongly the antiferromagnetic phase. Indeed, McWhan [5] has shown that the antiferromagnetic phase is completely suppressed by $P_c \approx 20$ kbar, which signals a remarkable high compressibility of the low-temperature Ni–S equilibrium bond length.

## 4. Oxides of nickel

Whereas NiS is metallic and oxidation leads to the formation of the disulfide ion in $NiS_2$, NiO is a classical antiferromagnetic insulator with a localized-electron $\mu_{Ni} = 1.8\mu_B$, albeit with a relatively high Néel temperature $T_N = 520$ K [6]. In order to obtain a metallic nickel oxide, it is necessary to go to trivalent nickel with a Ni–O–Ni bond angle approaching 180°. $NaNiO_2$ has an ordered rock-salt structure with $Na^+$ and $Ni^{3+}$ ions occupying alternate (111) planes of octahedral sites. In this non-metallic compound, the Ni–O–Ni bond angle 90° and the $Ni^{3+}$ ions carry a magnetic moment $\mu_{Ni} = 1\mu_B$. The rhombohedral perovskite $LaNiO_3$, on the other hand, is metallic and Pauli paramagnetic [6]. We may therefore expect to observe a transition from strongly to weakly correlated electronic behavior at some critical angle $\phi$ of a $(180° - \phi)$ Ni–O–Ni bond angle. However, before turning to an illustration of this transition, two side remarks are useful.

### 4.1. Charge-transfer gaps

Analysis of photoelectron-spectroscopy (PES) data

has been well-served by an ionic model in which a distinction is made between a charge-transfer gap $\Delta$ and a correlation gap $U$ between the lowest unoccupied redox energy and the highest occupied state [7]. In this model, NiO is said to have a charge-transfer gap $\Delta$ between the top of an $O^{2-}$:$2p^6$ valence band and the empty $Ni^{2+}/Ni^{+}$:$3d^9$ redox energy; a calculated correlation gap $U > \Delta$ between the $Ni^{3+}/Ni^{2+}$ and $Ni^{2+}/Ni^{+}$ energies would place the occupied $Ni^{3+}/Ni^{2+}$:$3d^8$ level well below the top of the $O^{2-}$:$2p^6$ valence band as indicated by the dotted peak in the density of states profile of Fig. 2. However, representation of the ground-state properties of NiO requires introduction of a strong hybridization between O-2p and Ni-3d states. This hybridization raises a narrow band of antibonding states to the top of the valence band to make $U_{eff} = \Delta$ with a Ni(III)/Ni(II) redox couple containing a strong admixture of Ni-3d and O-2p states. The spin degeneracy is removed from the antibonding states at the top of the valence band. These are $\sigma^*$ states of Ni-e and O-2$p_\sigma$ e-orbital parentage as the $\sigma$-band interactions are stronger than the $\pi$-bond interactions.

Oxidation of $Ni^{2+}$ ions in an oxide lowers the Fermi energy $\epsilon_F$ into the narrow band of antibonding $\sigma^*$ states at the top of the valence band, so the Ni is in a low-spin state, Ni(III):$t_2^6\sigma^*$ [1]. However, 90° Ni–O–Ni interactions are between orthogonal $\sigma^*$ orbitals, so the bandwidth remains narrow and the Ni(III) carry a localized magnetic moment in $NaNiO_2$. In the perovskite structure with a $(180° - \phi)$ Ni–O–Ni bond angle, the overlap integral varies as $\cos\phi$ and the tight-binding bandwidth becomes [6]

$$W_\sigma = \tfrac{1}{2} z b_\sigma = \epsilon_\sigma \lambda_\sigma^2 \cos\phi \qquad (4)$$

where $\epsilon_\sigma$ is a one-electron energy, $z = 6$ is the number of Ni near neighbors to a Ni atom and $\lambda_\sigma$ is the covalent-mixing parameter associated with hybridization of the Ni-e and O-2$p_\sigma$ orbitals. In Eq. (4), the hybridization is treated in second-order perturbation theory, which may not be appropriate; but the expression reveals the essence of the hybridization process. What required quantization is the proportion of Ni-e and O-2$p_\sigma$ character in the $\sigma^*$ band. Equation (4) reveals that, if $\lambda_\sigma$ is large enough for itinerant-electron behavior with $\phi = 0°$, there must be a critical angle $\phi$ at which there is a transition from itinerant ($\mu_{Ni} = 0$) to strongly correlated ($\mu_{Ni} > 0$) electronic behavior.

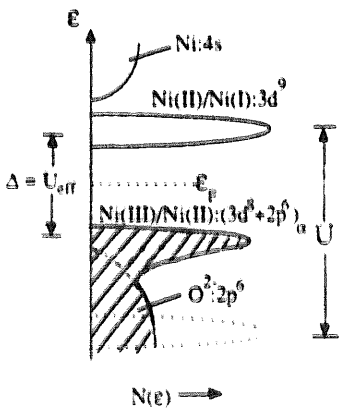


Fig. 2. Schematic energy density of states $N(\epsilon)$ for NiO.

### 4.2. Perovskites

The ideal $AMO_3$ perovskite structure of Fig. 3 contains M–O and A–O bond lengths that are matched only for a tolerance factor

$$t \equiv (A\text{–}O)/\sqrt{2}(M\text{–}O) \qquad (5a)$$

of unity. A $t < 1$ places the M–O bonds under compression and the A–O bonds under tension; a $t > 1$ does the opposite. Nature accommodates to a $t < 1$ by a cooperative rotation of the corner-shared $MO_6$ octahedra. Rotations about a [111] axis reduce the symmetry from cubic to rhombohedral, about a [110] to orthorhombic and about an [001] to tetragonal. These rotations all bend the M–O–M bond angle from 180°, and the angle $\phi$ of the $(180° - \phi)$ M–O–M bond angle can be increased by decreasing the mean size of the A cation. Moreover, the A–O and M–O bonds have different thermal-expansion coefficients and different compressibilities, which means that the tolerance factor $t = t(T,P)$ is dependent on both temperature and pressure. In general, the A–O bond has the larger thermal-expansion coefficient, which gives a $\partial\phi/\partial T < 0$. We can expect a cross-over from localized to itinerant electronic behavior would be found with increasing temperature. Normally the A–O bond is softer than an M–O bond for a transition-metal atom M, as has been demonstrated [8] by the pressure dependence of the hexagonal $AMO_3$ polytypes with $t > 1$. However, an anomalously high compressibility of an $\langle M\text{–}O\rangle_{local}$ near a transition from localized to itinerant electron behavior makes $t$ increase with pressure to give a $\partial\phi/\partial P < 0$. It is customary to calculate $t$ for room temperature and ambient pressure from A–O and M–O bond lengths obtained by summing the empirical ionic radii given in tables.

A second important feature of the perovskite structure is the possibility of creating shorter and longer M–O bonds by a displacement of the oxygen atoms along a bond axis. Shorter M–O bonds increase the crystalline field, i.e. the local Madelung energy $E_m$, at the cation as well as the covalent mixing parameters, so the antibonding states associated with shorter M–O bonds have a higher energy than those associated

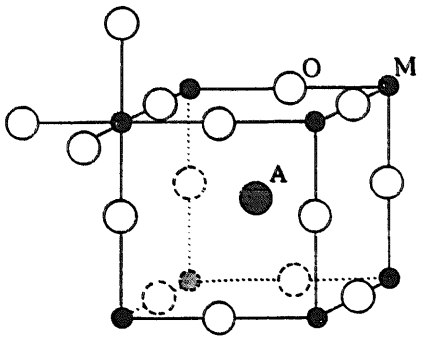


Fig. 3. Ideal cubic $AMO_3$ perovskite structure.

with longer M–O bonds. Moreover, accommodations of the M–O–M bond angles to give a smaller $\phi$ in domains of shorter ⟨M–O⟩ bond lengths and a larger $\phi$ in domains of longer ⟨M–O⟩ bond lengths allows a variety of cooperative oxygen displacements to be stabilized, and these cooperative displacements may be either static or dynamic. The nickel oxides with the perovskite structure provide an illustration.

Figure 4 shows that the transition from an antiferromagnetic semiconductor to a Pauli-paramagnetic metal occurs at a transition temperature $T_t$ that increases sharply with decreasing room-temperature tolerance factor [9a,9b], i.e. as the bending angle $\phi$ of the Ni–O–Ni bonds increases. The transition is first-order and the antiferromagnetic pase $NdNiO_3$ decreases sharply with pressure [10a,10b]. However, unlike NiS, the magnetic order below $T_N$ is not a simple antiferromagnetic coupling of nearest-neighbor nickel-atom moments; ferromagnetic (111) planes of nickel atoms are alternatively coupled ferromagnetically and antiferromagnetically. Since the narrow $\sigma^*$ band is one-quarter filled, a global transition to strongly correlated electrons could be expected to give ferromagnetic order. The nature of the magnetic order clearly signals stabilization below $T_N$ of both a charge-density wave (CDW) and a spin-density wave (SDW) propagating along a [111] direction perpendicular to the ferromagnetic (111) planes with propagation vectors $\mathbf{q}_{SDW} = 2\mathbf{q}_{CDW}$. An interpretation of this order is that the CDW represents a static phase segregation into itinerant-electron, ferromagnetic Ni–O–Ni sheets that are coupled antiferromagnetically to one another across an oxide-ion (111) plane by a Ni–O–Ni superexchange interaction [11]. Formally it is simplest to visualize stabilization of $Ni^{2+}$ valence states with alternating (111) planes of $O^-$ and $O^{2-}$ ions, which would correspond to a CDW. Within the ferromagnetic blocks the nickel moments would be coupled ferromagnetically by a covalent $Ni^{2+}:(\uparrow)–O^-(\downarrow)–Ni^{2+}(\uparrow)$ exchange whereas superexchange $Ni^{2+}:(\uparrow)–O^{2-}(\downarrow\uparrow)–Ni^{2+}(\downarrow)$ interactions couple adjacent blocks antiferromagnetically. This situation may be considered a static phase segregation into strongly correlated, itinerant-electron blocks coupled by localized-electron ionic bonding. This model predicts a smaller angle $\phi$ and ⟨Ni–O⟩ bond length in the ferromagnetic sheets compared to the ⟨Ni–O⟩ bond lengths and bending angle $\phi$ in the alternate blocks.

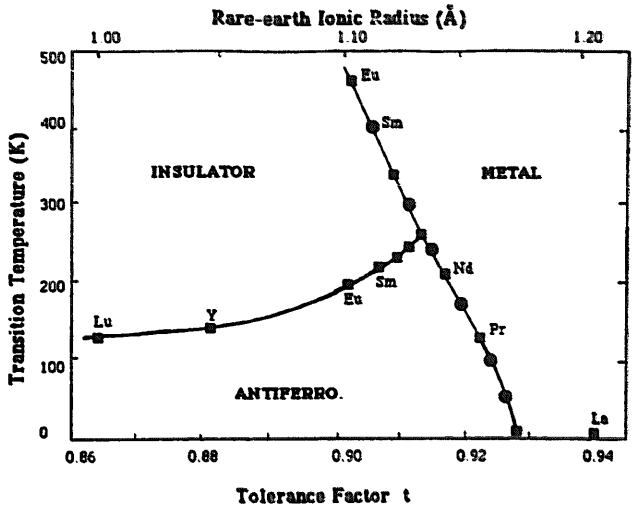


Fig. 4. Transition temperatures vs. tolerance factor $t$ for the $RNiO_3$ pervoskites [9a,9b].

## 5. Coexistence of localized spins and itinerant electrons

Implicit in the de Gennes [12] model of the Zener [13] double-exchange interaction in the $La_{1-x}Sr_xMnO_3$ system is the assumption that itinerant and localized 3d electrons may coexist on the same transition-metal atom. Nevertheless, the explicit identification [14] of where this phenomenon may be found has received little recognition by the theoretical community. Three examples are instructive.

### 5.1. Troilite [15]

The atomic potentials experienced by majority-spin and minority-spin electrons at a transition-metal atom are not the same, the maximum difference occurring for a high-spin $d^6$ configuration. At a transition from localized to itinerant electronic behavior, the minority-spin electrons may become delocalized before the majority-spin electrons. This case is illustrated by troilite, the high-spin form of FeS. Troilite has the $B8_1$ structure of NiAs above a spin-flip temperature $T_s < T_N = 325°C$. Below the Néel temperature $T_N$, the high-spin $Fe^{2+}$ ion magnetic moments become coupled parallel to one another within close-packed (001) planes of octahedral sites, but the planes are coupled antiparallel to one another. The majority-spin $d^5_\alpha$ configuration is localized with a spin $S = 5/2$, and the magnetic order remains unchanged below $T_N$ through

two crystalline transitions that reveal a transition to non-localized character of the minority-spin electrons. On cooling, the first transition occurs at $T_s$ where the structure transforms from the hexagonal $B8_1$ to the orthorhombic B31 phase in which the Fe atoms are displaced cooperatively to form zig-zag chains of shorter Fe–Fe separations within a close-packed basal plane. A $B31 \rightleftharpoons B8_1$ transition may be induced by either Fe–Fe or S–S interactions. On further cooling, a first-order phase change occurs at a $T\alpha \approx 150$°C below which the $\beta$-spin electrons become trapped in three-ion triangular clusters within the close-packed Fe-atom planes. The Fe-atom displacements create an Fe–Fe separation of 3.00 Å within a cluster and 3.73 Å between clusters. This transition indicated that the Fe–Fe interactions are dominant in troilite. The minority-spin electron of $Fe^{2+}$ ion occupies a triangular molecular orbital below $T\alpha$ whereas the majority-spin $d^5_\alpha$ configuration remains localized.

### 5.2. $LaCoO_3$ [16]

In the perovskite structure, a larger overlap of the M-e and O-$2p_\sigma$ orbitals than to the M-t and O-$2p_\pi$ orbitals gives bandwidths $W_\sigma > W_\pi$ and on-site electrostatic energies $U_\pi > U_\sigma$. Therefore the cross-over condition $W_\sigma \approx U_\sigma$ for formation of a $\sigma^*$ band of itinerant-electron states occurs where a $W_\pi > U_\pi$ retains a localized-electron $t^n$ configuration with, for $3 \leq n < 5$, a localized spin $S = (6-n)/2$. This situation is illustrated in $LaCoO_3$ and the mixed-valent systems $Ln_{1-x}A_xMnO_3$ with Ln = rare earth and A = alkaline-earth atoms.

The Co(III) ions in the perovskite $LaCoO_3$ all have the low-spin configuration $t^6e^0$ at lowest temperatures. On increasing the temperature in the range $0 < T \leq 100$ K, an increasing number of cobalt ions are converted to a high-spin, localized-electron $Co^{3+}$:$t^4e^2$ state with a spin $S = 2$. Introduction of electrons into antibonding e orbitals increases significantly the Co–O bond length at a high-spin $Co^{3+}$ ion, so the oxide ion of a $Co^{3+}$–O–Co(III) bond becomes displaced toward the Co(III) ion. These displacements stabilize Co(III) as near neighbors of $Co^{3+}$ ions, and there is a dynamic short-range ordering of high-spin and low-spin configurations on alternate cobalt sites in the range ordering of high-spin and low-spin configurations on alternate cobalt sites in the range $110 \leq T \leq 350$ K. As the temperature is increased further, the electron transfer rate between $Co^{3+}$ and Co(III) ions becomes faster than the period of an oxygen vibration along the bond axis, and electron transfers $t^6e^0 + t^4e^2 \rightleftharpoons 2t^5\sigma^{*1}$ stabilize domains of like cobalt atoms in intermediate-spins states with itinerant $\sigma^*$ electrons coexisting with localized $t^5$ configurations. The Fermi energy $\epsilon_F$ of the $\sigma^*$-band electrons lies in the gap $U_\pi$ between the localized $t^5$ and $t^6$ configurations [14]. The Hund intraatomic exchange field removes the $\sigma^*$-band spin degeneracy at a cobalt atom, so the intermediate-spin cobalt atoms carry an effective spin $S = 1$. The volume of the intermediate-spin domains increases with temperature until the system has a homogeneous intermediate-spin configuration above approx. 650°C. Substitution of Sr for La in the system $La_{1-x}Sr_xCoC_3$ initially created superparamagnetic intermediate-spin domains stable to lowest temperatures; and for $0.30 \leq x \leq 0.50$, a percolation path through the solid of the intermediate-spin domains gives ferromagnetic order below a Curie temperature $T_C$ with a spontaneous magnetization approaching $(2-x)\mu_B$ cobalt by $x = 0.5$ [17].

### 5.3. $Ln_{1-x}A_xMnO_3$

The mixed-valent $Ln_{1-x}A_xMnO_3$ perovskites provide a final example. $LaMnO_3$ has a tolerance factor $t < 1$ that stabilizes a cooperative rotation of the $MnO_6$ octahedra about [110] axes to reduce the symmetry from cubic to orthorhombic. The $Mn_{3+}$ ions of $LaMnO_3$ all have localized, high-spin configurations $t^3e^1$; the twofold e-orbital degeneracy is removed at lower temperatures by a cooperative Jahn–Teller deformation that creates short O–Mn–O bonds alternating with long O···Mn···O bonds in the (001) planes, each $Mn^{3+}$ ion having long bonds at right angles to short bonds. Uniform Mn–O bond lengths along the $c$-axis have a Mn–O–Mn bond length that is shorter than the Mn···O–Mn bond lengths of a basal plane, which makes $c/a < \sqrt{2}$. Normally, orthorhombic perovskites have a $c/a > \sqrt{2}$. It is convenient to distinguish the O′-orthorhombic phase with $c/a < \sqrt{2}$ from an O-orthorhombic phase with $c/a > \sqrt{2}$ [18].

For all values of $x$ as well as lanthanide ion $Ln^{3+}$ and alkaline-earth ions $A^{2+}$, the manganese ions retain a localized $t^3$ configuration with a spin $S = 3/2$; the $t^3$–O–$t^3$ superexchange interactions are antiferromagnetic, but weaker than the ferromagnetic $e^1$ ···O–$e^0$ $Mn^{3+}$ ···O–$Mn^{3+}$ superexchange interactions [19], so the (001) planes become ferromagnetic below a Néel temperature $T_N$. However, the Jahn–Teller ordering of the e electrons into long Mn···O bond within the (001) planes leaves $e^0$–O–$e^0$ interactions along the $c$-axis, so the antiferromagnetic $t^3$–O–$t^3$ interactions couple the ferromagnetic (001) planes antiferromagnetic along the $c$-axis [20]. A Dzialoskinskii antisymmetric exchange cants the spins to give a weak ferromagnetic component perpendicular to the orthorhombic $b$-axis.

Substitution of La by alkaline earth oxidizes the $MnO_3$ array and introduces $Mn^{3+}$–O–$Mn^{4+}$ ⇌ $Mn^{4+}$–O–$Mn^{3+}$ double-exchange interactions resulting from a real e-electron charge transfer in a time

short compared to the period of an oxygen-atom vibration between the Mn atoms; superexchange interactions involve a weaker virtual charge transfer. The e-electron participating in double-exchange interactions occupy either a molecular orbital within a cluster of two or more Mn atoms of a $\sigma^*$-band state; holes in the $Mn^{4+}/Mn^{3+}$ redox couple induce either a local or a global delocalization of the e electrons while leaving the $t^3$ configurations localized. Nevertheless, the e-orbital degeneracy constrains the double-exchange interaction to be directional with a cluster; and unless the $Mn^{3+}$–O–$Mn^{4+}$ molecular orbital can reorient its direction in a time short compared to the period of the oxygen displacements, the cluster is polaronic and moves diffusively. In order for the double-exchange component to influence every Mn–O–Mn interaction, the mobility of a $Mn^{4+}$ ion must create a mean free path comparable to the $Mn^{4+}$-ion separations during the spin-relaxation time.

Figure 5 compares the phase diagram [21,22] for $La_{1-x}Sr_xMnO_3$ with that [23] for $Ln_{0.7}A_{0.3}MnO_3$ with the $Ln^{3+}$ and $A^{3+}$ ions chosen to vary the tolerance factor $t$ for a fixed Mn(IV)/Mn ratio. Attention is restricted to the remarkable variation of $T_c$ with the factor $t$ that is quite independent of the Mn(IV)/Mn ratio $x$. We distinguish three regions in these phase diagrams: $t = < 0.96$, $0.96 \leq t < 0.98$ and $t \geq 0.98$.

(i) For $t \geq 0.98$, the structure is rhombohedral; cooperative rotations of the $MnO_6$ octahedra about [111] axes give a smaller bending angle $\phi$ of the $(180° - \phi)$ Mn–O–Mn bond than is found in the orthorhombic phase. Moreover, the rhombohedral symmetry is not compatible with a cooperative Jahn–Teller deformation. In this structure, the e electrons appear to occupy itinerant-electron states of a narrow $\sigma^*$ band below $T_c$ whereas the $t^3$ configurations remain localized. The width of the $\sigma^*$ band is given, in tight-binding approximation, by

$$W_\sigma \approx 12\epsilon_\sigma \lambda_\sigma^2 \cos\phi < \cos(\theta_{ij}/2) > \quad (5b)$$

where the spin-independent resonance integral $b_\sigma$ of Eq. (4) has been replaced by a spin-dependent integral $t_\sigma = b_\sigma \cos(\theta_{ij}/2)$; $\theta_{ij}$ is here the angle between the spins of a $Mn^{3+}$–O–$Mn^{4+}$ cluster and a neighboring $Mn^{3+}$ atom. Replacement of $b_\sigma$ by $t_\sigma$ is required because of the presence of localized $t^3$ configurations to which the mobile e-electron spins are strongly coupled by Hund's intraatomic-exchange field.

Above $T_c$, polaronic clusters form, but they move with a motional enthalpy $\Delta H_m < kT$ that has a high enough mobility to give a global double-exchange interaction. This assertion is supported by Fig. 6, which shows the inverse paramagnetic-susceptibility data and the corresponding thermoelectric power for $LaMnO_3$ and several $Ln_{0.7}A_{0.3}MnO_3$ samples. In this figure, the $La_{0.7}Ba_{0.3}MnO_3$ sample has a $t > 0.98$. Two features of the curves for $La_{0.7}Ba_{0.3}MnO_3$ are to be noted: (a) at high temperatures, the Seebeck coefficient is temperature-independent with a value $\alpha \approx -20\ \mu V/K$ and (b) the paramagnetic susceptibility obeys a Curie–Weiss law with a Curie constant described by individual $Mn^{4+}$ and high-spin $Mn^{3+}$ ions and with a Weiss constant $\theta = T_c + \Delta T$ where $\Delta T$ is not anomalously large. A temperature-independent $\alpha$ signals polaronic behavior with a dominant statistical contribution to the thermopower given by

$$\alpha = -(k/e)\ln[\beta(1-c)/c] \quad (6)$$

where $\beta$ is a spin-degeneracy factor and $c = x/N'$ is the fraction of available sites that are occupied by a mobile charge carrier. Use of a $\beta = 2$ and a small-polaron $N' = 1$, corresponding to the number of Mn atoms per formula unit, requires an oxygen stoichiometry $O_{3.10}$ to obtain an $\alpha = -20\ \mu V/K$ as compared to a measured $O_{2.98}$, which is outside the exper-

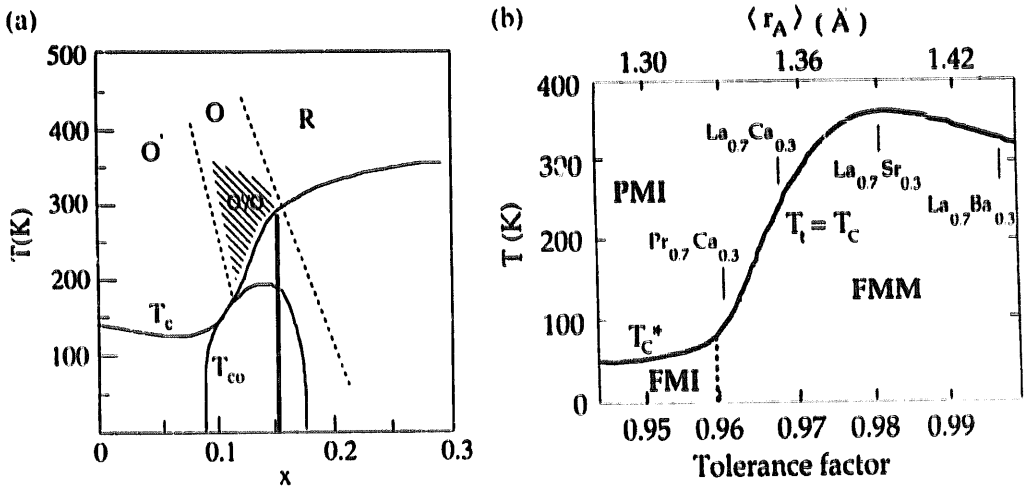


Fig. 5. Phase diagrams for (a) $La_{1-x}Sr_xMnO_3$ and (b) $La_{0.7}A_{0.3}MnO_3$ vs. tolerance factor $t$.

imental error. Given the strong Hund intraatomic-exchange field, removal of the spin degeneracy can be expected to give a $\beta = 1$, in which case an $N' = 1$ would give $\alpha = +38\ \mu V/K$ whereas $N' = 1/2$ gives the measured $\alpha = -20\ \mu V/K$. Apparently the holes move as two-manganese clusters above $T_c$ even though the mobility of a hole is rapid enough to give a $\theta$ corresponding to a uniform distribution of double-exchange interactions and a Curie constant described by individual $Mn^{4+}$ and high-spin $Mn^{3+}$ ions. Here segregation into molecular clusters and localized e electrons is dynamic. The domain of short-range ferromagnetic order, $\Delta T = \theta - T_c$, shows little evidence of a trapping out of superparamagnetic $Mn^{3+}$–O–$Mn^{4+}$ dimeric units above $T_c$, and below $T_c$ the $\sigma^*$ electrons are itinerant.

(ii) For $t < 0.96$, the system remains polaronic both above and below $T_c$. The $(Nd_{0.5}Sm_{0.5})_{0.7}Ca_{0.3}MnO_3 (t < 0.96)$ curve of Fig. 6 shows semiconductive behavior; and $\alpha = -3 \pm 5\ \mu V/K$ at high temperatures indicates the coexistence of single-site and dimeric small polarons. The paramagnetic susceptibility deviates strongly from Curie–Weiss behavior with an effective Curie constant that increases with decreasing temperature as though short-range ferromagnetic order extended from a $T_c \approx 100$ K to nearly 600 K. This behavior suggests that the dimeric polarons have a relatively small mobility so that they form superparamagnetic clusters that become increasingly trapped out into larger ferromagnetic domains on lowering the temperature to $T_c$.

(iii) The range $0.96 \leq t < 0.98$ is transitional. It is represented in Fig. 6 by the compositions $(La_{1-x}Nd_x)_{0.77}Ca_{0.3}MnO_3$. At highest temperatures, an $\alpha = -20\ \mu V/K$ signals the presence of dimeric $Mn^{3+}$–O–$Mn^{4+}$ polarons with a high mobility

$$\mu_e \sim \omega_o \exp(-\epsilon_p/W_\sigma)\exp(-\Delta H_m/kT) \quad (7)$$

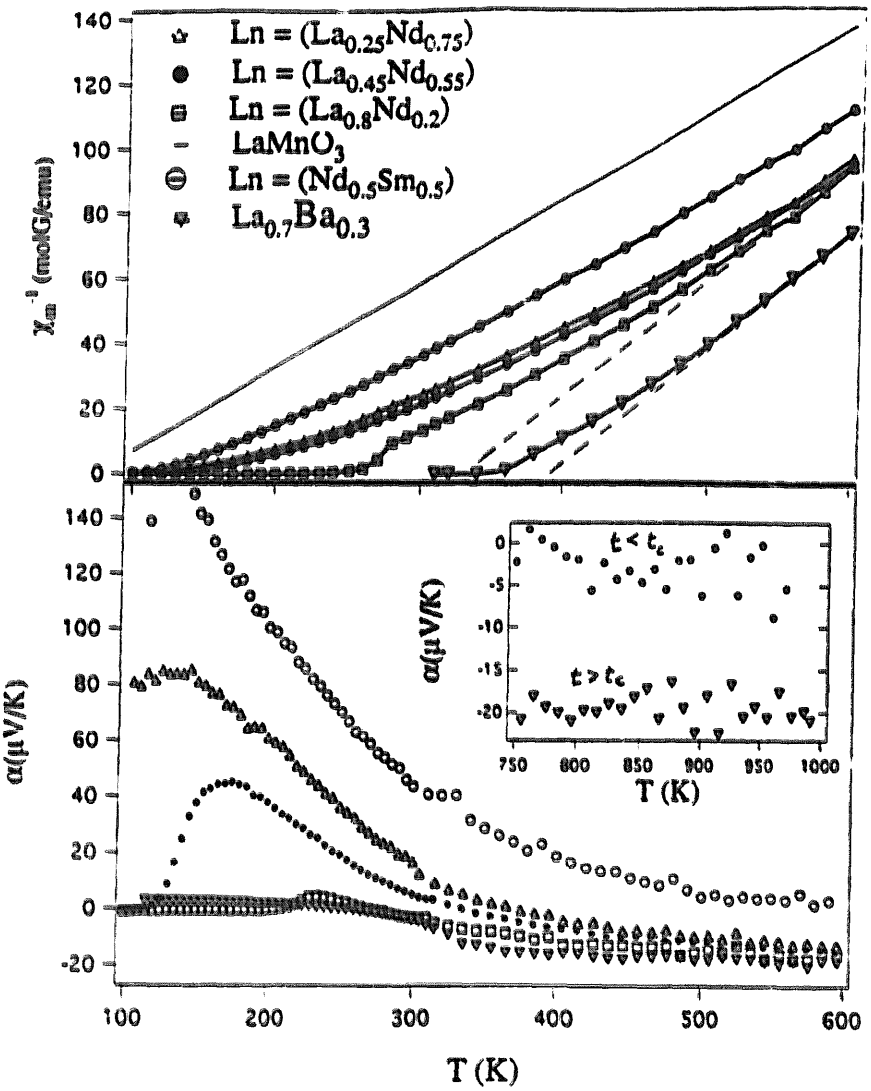


Fig. 6. Inverse paramagentic susceptibility $\chi_m^{-1}(T)$ and Seebeck coefficient $\alpha(T)$ for $Ln_{0.7}Ca_{0.3}MnO_3$ and $La_{0.7}Ba_{0.3}MnO_3$; solid line represents for $\chi_m^{-1}(T)$ $LaMnO_3$.

because of a motional enthalpy $\Delta H_m < kT$. The ratio $\epsilon p/W_\sigma$ of the polaron-formation energy to the $\sigma^*$ bandwidth increases with decreasing $t$ in the interval $0.96 \le t < 0.98$; and as $t$ decreases, there is an increased trapping out below room temperature of the mobile charge carriers into short-range ferromagnetic domains, which lowers $T_c$ of the matrix. The result is a large $\Delta T = \theta - T_c$ that increases with decreasing $T$ with heterogeneous mixture of ferromagnetic domains in a paramagnetic matrix. Small-angle neutron scattering (SANS) data [24] have revealed the presence of ferromagnetic domains with 10–20 Å coherence length that increase in volume with the application of a magnetic field. Formation of these domains represents phase segregation into hole-rich and hole-poor domains as a result of cooperative oxygen-atom displacements. Moreover, substitution of $^{18}O$ for $^{16}O$ causes $T_c$ to drop remarkably for compositions $0.96 \le t < 0.98$, a change as high as $\Delta T_c = -21°C$ being reported [25]. This change is due to a reduction in the cluster mobility, which reduces the double-exchange component to the matrix interatomic-exchange field. Increased trapping out of the mobile charge carriers with decreasing bandwidth $W_\sigma$, and their subsequent release on increasing $\langle\cos(\theta_{ij}/2)\rangle$ either by the application of a magnetic field above $T_c$ or by the internal molecular field below $T_c$ [26] results in intrinsic colossal magnetoresistance (CMR) above $T_c$ due to the release of trapped charge carriers has been shown [27] to be compensated by the loss in spin entropy, and the release of charge carriers below $T_c$ occurs progressively, not discontinuously, with decreasing $T$.

Finally, the vanishing of $\alpha$ below $T_c$ that is seen in Fig. 6 for $(La_{0.45}Nd_{0.55})_{0.7}Ca_{0.3}MnO_3$ signals the stabilization of an unusual electronic state [28]. Measurement [21] of the transport properties of a single crystal of $La_{0.85}Sr_{0.15}MnO_3$ as a function of hydrostatic pressure has revealed a transition from polaronic itinerant behavior of the $\sigma^*$ electrons in the pressure range $5 < P < 6$ kbar, and Louca et al. [29] have used pulsed neutron diffraction to detect the presence of three-manganese-center clusters below $T_c$. A low $\alpha$ can be reconciled with such clusters since a twofold orbital degeneracy at a $Mn^{4+}$ within a three-manganese cluster gives $N' = 2/3$ and Eq. (6) reduces to $\alpha = 0$ for $\beta = 1$, $x = 0.33$, and $N' = 2/3$. Here the double-exchange component of the ferromagnetic interatomic-exchange interaction appears to depend on the mobility of the polaronic clusters.

## Acknowledgements

The National Science Foundation and the Robert A. Welch Foundation, Houston, TX, are thanked for financial support and J.-S. Zhou for permission to use Fig. 6.

## References

[1] J.B. Goodenough, Some Comparisons of Flourides, Oxides and Sulfides containing Divalent Transition Elements in: C.N.R. Rao (Ed.), Proc. Winter School in Solid State Chemistry IIT, Kanpur, India, December 1971, Marcel Dekkar, New York, 1993, p. 288.
[2] R.B. Lindsay, Physical Mechanics, D. van Nostrant, New York, 1993, p. 288.
[3a] J.T. Sparks, T. Komoto, Phys. Lett. 15A (1967) 398.
[3b] J.T. Sparks, T. Komoto, Revs. Mod. Phys. 40 (1968) 752.
[4] J. Trahan, R.G. Goodrich, S.F. Watkins, Phys. Rev. B 2 (1970) 2859.
[5] D. McWhan (private communication, 1970).
[6] J.B. Goodenough, Prog. Solid State Chem. 5 (1971) 145.
[7] J. Zaanen, G.A. Sawatzky, J.W. Allen, Phys. Rev. Lett. 55 (1985) 418.
[8] J.B. Goodenough, J.A. Kafalas, J.M. Longo, in: P. Hagenmuller (Ed.), Preparative Methods in Solid State Chemistry, Academic Press, New York, 1972, Ch. 1.
[9a] J.B. Torrance, P. Lacorre, A.I. Nazzal, E.J. Ansaldo, Ch. Niedermayer, Phys. Rev. B45 (1992) 8209.
[9b] J.L. Garcia-Muñox, J. Rodriguez-Carvajal, P. Lacorre, Europhys. Lett. 20 (1992) 241.
[10a] X. Obradors, L.M. Paulius, M.B. Maple, J.B. Torrance, A.I. Nazzal, J. Fontcuberta, X. Granados, Phys. Rev. B47 (1993) 12353.
[10b] P.C. Canfield, J.D. Thompson, S.-W. Cheong, L.W. Rupp, Phys. Rev. B47 (1993) 12347.
[11] J.B. Goodenough, J. Solid State Chem. 127 (1996) 126.
[12] P.G. deGennes, Phys. Rev. 118 (1960) 141.
[13] C. Zener, Phys. Rev. 82 (1951) 403.
[14] J.B. Goodenough, Mater. Res. Bull. 6 (1971) 967.
[15] J.B. Goodenough, Ann. Chim. Fr. 7 (1982) 489.
[16] M.A. Señaris-Rodriguez, J.B. Goodenough, J. Solid State Chem. 116 (1995) 224.
[17] M.A. Señaris-Rodriguez, J.B. Goodenough, J. Solid State Chem. 118 (1995) 323.
[18] J.B. Goodenough, J.M. Longo, Landolt-Börnstein, in: H. Hellwege (Ed.), Tabellen New Series, Group III/4a, Springer-Verlag, Berlin, 1970, p. 126.
[19] J.B. Goodenough, Phys. Rev. 100 (1955) 564.
[20] E.O. Wollan, W.C. Koeheler, Phys. Rev. 100 (1955) 545.
[21] J.-S. Zhou, J.B. Goodenough, A. Asamitsu, Y. Tokura, submitted.
[22] Y. Yamada, O. Hino, S. Nolido, R. Kanao, Phys. Rev. Lett. 77 (1996) 904.
[23] H.Y. Hwang, S.-W. Cheong, P.G. Radaelli, M. Marezio, B. Batlogg, Phys. Rev. Lett. 75 (1995) 914.
[24] J.M. De Teresa, M.R. Ibarra, P.A. Algarabel, C. Ritter, C. Marqnina, J. Blasco, J. Garcia, A. del Moral, Z. Arnold, Nature (London) 386 (1997) 256.
[25] G.-M. Zhao, K. Conder, H. Keller, K.A. Mueller, Nature (London) 381 (1996) 676.
[26] W. Archibald, J.-S. Zhou, J.B. Goodenough, Phys. Rev. B53 (1996) 15555.
[27] N. Overend, quoted by J.B. Goodenough, J. Appl. Phys. 81 (in press).
[28] J.-S. Zhou, W. Archibald, J.B. Goodenough, Nature (London) 381 (1996) 770.
[29] D. Louca, T. Egami, E.L. Brosha, M. Röder, A.R. Bishop, Phys. Rev. Lett. (submitted).